Replacing nonmuscle myosin 2A with myosin 2C1 permits gastrulation but not placenta vascular development in mice

Yingfan Zhang[a], Chengyu Liu[b], Robert S. Adelstein[a], and Xuefei Ma[a,*]
[a]Laboratory of Molecular Cardiology and [b]Transgenic Core, National Heart, Lung, and Blood Institute, National Institutes of Health, Bethesda, MD 20892-1583

ABSTRACT **Three paralogues of nonmuscle myosin 2 (NM 2A, 2B, and 2C) are expressed in mammals, and the heavy chains are the products of three different genes (Myh9, Myh10, and Myh14, respectively). NM 2A and 2B are essential for mouse development, while 2C is not. Studies on NM 2C are limited and the in vivo function of this paralogue is not clear. Using homologous recombination, cDNA encoding nonmuscle myosin heavy chain 2C1 fused with GFP was introduced into the first coding exon of Myh9, replacing NM 2A expression with NM 2C1 expression in mice. In contrast to A^{-}/A^{-} embryos, which die by embryonic day (E) 6.5, A^{C1*gfp}/A^{C1*gfp} embryos survive through E8.5, demonstrating that NM 2C1 can support mouse development beyond gastrulation. At E9.5 and E10.5, however, A^{C1*gfp}/A^{C1*gfp} embryos are developmentally delayed, with abnormalities in placental vascular formation. The defect in vascular formation is confirmed in allantois explants from A^{C1*gfp}/A^{C1*gfp} embryos. Thus, NM 2C1 cannot support normal placental vascular formation. In addition, A^{C1*gfp}/A^{C1*gfp} mouse embryonic fibroblasts (MEFs) migrate rapidly but with impaired persistence and develop smaller, less mature focal adhesions than A^{+}/A^{+} MEFs. This is attributed to enhanced NM 2C1 actomyosin stability and different NM 2C1 subcellular localization than in NM 2A.**

Monitoring Editor
William Bement
University of Wisconsin

Received: Dec 11, 2017
Revised: Jul 11, 2018
Accepted: Jul 17, 2018

INTRODUCTION

Nonmuscle myosin 2 (NM 2), a major component of the actomyosin cytoskeletal complex, plays important roles in a variety of basic cellular processes including cell polarity, cell migration, cell–cell adhesion, and cytokinesis (Robinson and Spudich, 2004; Vicente-Manzanares *et al.*, 2009; Heissler and Manstein, 2013). In mammals there are three NM 2 paralogues, each composed of a pair of nonmuscle myosin heavy chains (NMHCs) encoded by three different genes (*Myh9*, *Myh10*, *Myh14*), which together with two pairs of myosin light chains are referred to as NM 2A, 2B, and 2C. Though the three NM 2 paralogues show considerable homology in primary structure (~60% identity in amino acids), are similar in three-dimensional protein structure, and have overlapping cellular functions, their overall spatial and temporal expression profiles are quite different. These differences persist despite the ability of the paralogues to form cofilaments (Beach *et al.*, 2014).

Germline ablation of two of the three paralogues, NM 2A and NM 2B, in mice results in embryonic lethality with markedly different phenotypes. Ablation of NM 2A results in death by embryonic day (E) 6.5, with a defect in cell adhesion and visceral endoderm formation (Conti *et al.*, 2004). Ablation of NM 2B results in lethality by E14.5, accompanied by cardiac and brain abnormalities (Tullio *et al.*, 1997, 2001; Takeda *et al.*, 2003; Ma *et al.*, 2004). These results suggest that NM 2A and NM 2B have unique functions that are essential for mouse embryonic development. In contrast, germline ablation of NM 2C does not cause embryonic lethality or an apparently overt abnormal phenotype in mice (Ma *et al.*, 2010), raising the interesting and important question of whether NM 2C functions

This article was published online ahead of print in MBoC in Press (http://www.molbiolcell.org/cgi/doi/10.1091/mbc.E17-12-0713) on July 25, 2018.
The authors declare no competing financial interests.
Author contributions: Y.Z. and X.M. designed and performed experiments and prepared the manuscript; C.L. performed experiments; R.S.A. designed experiments and prepared the manuscript.
*Address correspondence to: Xuefei Ma (max@nhlbi.nih.gov).
Abbreviations used: BSA, bovine serum albumin; E, embryonic day; FBS, fetal bovine serum; GFP, green fluorescent protein; H&E, haemotoxylin and eosin; IgG, immunoglobulin G; NM, nonmuscle myosin; NMHC, nonmuscle myosin heavy chain; MEF, mouse embryonic fibroblast; PBS, phosphate-buffered saline; PFA, paraformaldehyde; siRNA, small interfering RNA.

redundantly or plays an ancillary role with the other two NM 2 paralogues in vivo.

Unlike NM 2A and NM 2B, which are expressed from the earliest stages of mouse embryonic development, NM 2C is not expressed until E11.5 (Golomb *et al.*, 2004; Ma *et al.*, 2010). Similarly to NMHC 2B, two alternative exons, C1 and C2, can be spliced into the mRNA, resulting in four NMHC 2C isoforms. NMHC 2C0 represents the noninserted form of NMHC 2C. The C1 insert encodes eight amino acids that can be incorporated into the ATP binding region at amino acid 227 to form NMHC 2C1 (Golomb *et al.*, 2004). The C2 insert encodes 41 amino acids that can be incorporated into the actin-binding region at amino acid 636 to form NMHC 2C2 (Jana *et al.*, 2009). The NM 2C isoforms differ in their actin-activated MgATPase activities, where the inclusion of either C1 or C2 enhances the MgATPase activity. Inclusion of the C2 insert results in NM 2C2 and NM 2C1C2 (containing both inserts), which are constitutively active and not regulated by the level of MLC20 phosphorylation (Jana *et al.*, 2009; Heissler and Manstein, 2011). NM 2C1 is the most widely expressed NM 2C isoform, found in a variety of tissues including liver, kidney, testes, brain, and lung (Golomb *et al.*, 2004).

Because most cells contain more than one NM 2, their specific roles during embryogenesis in vivo are unclear. Previous work has shown that some defects associated with the loss of NM 2B could be rescued in vivo by a motor-impaired 2B or even NM 2A when it was expressed from the NMHC 2B gene (Myh10) locus (Ma *et al.*, 2004, 2007; Bao *et al.*, 2007). These findings resulted in the hypothesis that the functions of NM 2 that involve cross-linking properties of actin filaments allow replacement by another paralogue, but those functions that are dependent on NM 2 motor activity are not substitutable because of differences in their kinetic properties. This hypothesis was also tested by genetic replacement in vivo of NM 2A by 2B or a mutant, motor-impaired 2A (Wang *et al.*, 2010; Zhang *et al.*, 2012). These studies revealed an important paralogue and motor-independent role of NM 2 in visceral endoderm development and a unique paralogue requirement for NM 2A instead of 2B in placenta development. NM 2A was also shown to be important in cell migration and focal adhesion formation in different cell lines including fibroblasts, cancer cell lines, and mouse hepatic stellate cells (Sandquist *et al.*, 2006; Even-Ram *et al.*, 2007; Liu *et al.*, 2011).

In this study, we tested whether NM 2C1 can substitute for NM 2A in vivo during mouse development. We used homologous recombination to ablate NMHC 2A by inserting cDNA encoding mouse NMHC 2C1-green fluorescent protein (GFP) fusion protein into the first coding exon of the NMHC 2A gene, exon2 of *Myh9*. This ablates NMHC 2A and places NMHC 2C1 under the control of the endogenous 2A promoter. We examined the mice generated following germ line transmission of the NMHC 2C1-GFP allele (designated as A^{C1*gfp}) with respect to the ability of NM 2C1 to replace the functions of NM 2A in mouse embryonic development. Our results show that while NM 2C1 can replace NM 2A during the critical developmental step of gastrulation, placenta vascular formation specifically requires NM 2A paralogue activity. In addition, we study the difference in properties between mouse embryonic fibroblasts (MEFs) containing NM 2A in the absence of NM 2C and those containing NM 2C1 in the absence of NM 2A.

RESULTS

Generation of the NM 2C1 replacement for NM 2A in mice

To generate the genetic NMHC 2C1 replacement for NMHC 2A in mice, exon2 of *Myh9*, which contains the NMHC 2A start codon, was targeted with mouse NMHC 2C1 cDNA fused at its 3′ end to the GFP sequence (Supplemental Figure S1A). Upon homologous recombination, NMHC 2A was ablated by the insertion of the NMHC 2C1-GFP sequence, which has its own stop codon, resulting in the expression of mouse NMHC 2C1-GFP under the control of the endogenous NMHC 2A promoter. Southern blotting and PCR analysis confirmed genetic replacement (Supplemental Figure S1, B and C). A floxed Neo^r cassette, which aided in selection of targeted clones, was removed by crossing the mutant mice with CMV-Cre mice. Homologous recombination was made easier by the presence of a "safe harbor" site in Myh9 (Liu *et al.*, 2018).

To confirm the replacement of NMHC 2A with NMHC 2C1 at the protein level, lung tissue extracts from 3-mo-old wild-type A^+/A^+ and heterozygous A^{C1*gfp}/A^+ mice were used for immunoblotting and showed a 50.4% (average of two immunoblots) decrease in NMHC 2A expression (Supplemental Figure S1D, row 1). As expected, an additional band with a molecular mass higher than that of the endogenous NMHC 2C was detected in the heterozygous A^{C1*gfp}/A^+ lung tissues with an NMHC 2C antibody directed to the N-terminus of NMHC 2C, indicating successful expression of NM 2C1-GFP in the mouse tissue (Supplemental Figure S1D, row 3). Immunoblotting with both anti-GFP and anti-NMHC 2C antibodies confirmed that this additional band is positive with both antibodies (Supplemental Figure S1D, row 4; row 2 is GAPDH, which is used as a loading control for row 1).

As Supplemental Figure S1D shows, prolonging SDS–PAGE enabled separation of the exogenous NMHC 2C1-GFP and the endogenous NMHC 2C and permitted quantification of the extent of NMHC 2C1-GFP expression under the control of the endogenous NMHC 2A promoter. Quantification of the immunoblots showed that the NMHC 2C1-GFP expression level is 43.2 ± 2.1% of the endogenous NMHC 2C ($n = 6$). Previous mass spectroscopy studies showed that wild-type mouse lung tissue contains almost equal amounts of NMHC 2A and NMHC 2C (Ma *et al.*, 2010). Therefore, with the promoter on one allele of Myh9 controlling the expression of 2C1-GFP in A^{C1*gfp}/A^+ lung tissues, the expression level of 2C1-GFP should be about half of the endogenous NMHC 2C expression level, as shown in Supplemental Figure S1D, row 3. Thus, in our mouse model, the expression level of NMHC 2C1-GFP under the control of the NMHC 2A promoter in A^{C1*gfp}/A^+ lung tissue is approximately the same as the expression level of endogenous NMHC 2A, and is neither over- nor underexpressed.

Immunoblot experiments were also carried out with protein extracts of A^+/A^+ and homozygous A^{C1*gfp}/A^{C1*gfp} MEFs cultured from E9.5 mouse embryos. NMHC 2A could not be detected in extracts from A^{C1*gfp}/A^{C1*gfp} MEFs (Supplemental Figure S1E). NMHC 2C is not normally expressed in wild-type MEFs but is detected in A^{C1*gfp}/A^{C1*gfp} MEFs. Using an antibody to GFP and an antibody to NMHC 2C, a single band was detected with a molecular mass higher than 250 kDa (Supplemental Figure S1E, row 2). These results confirm ablation of NMHC 2A and expression of 2C1-GFP in A^{C1*gfp}/A^{C1*gfp} MEFs.

Replacing NM 2A with NM 2C1 permits embryo survival beyond gastrulation but not placental vascular formation

Mating of A^{C1*gfp}/A^+ mice did not produce live homozygous A^{C1*gfp}/A^{C1*gfp} offspring. A^{C1*gfp}/A^{C1*gfp} embryos at E8.5 were normal in size and appearance compared with A^+/A^+ and A^{C1*gfp}/A^+ embryos. However, at E9.5, live A^{C1*gfp}/A^{C1*gfp} embryos were markedly smaller than wild-type littermates and were developmentally delayed (Figure 1A, left panel), indicated by the unturned embryo morphology, which differs from that of wild-type mouse embryos at E8.5 (unpublished data). At E10.5, some embryos were dead and undergoing resorption, and live A^{C1*gfp}/A^{C1*gfp} embryos were markedly

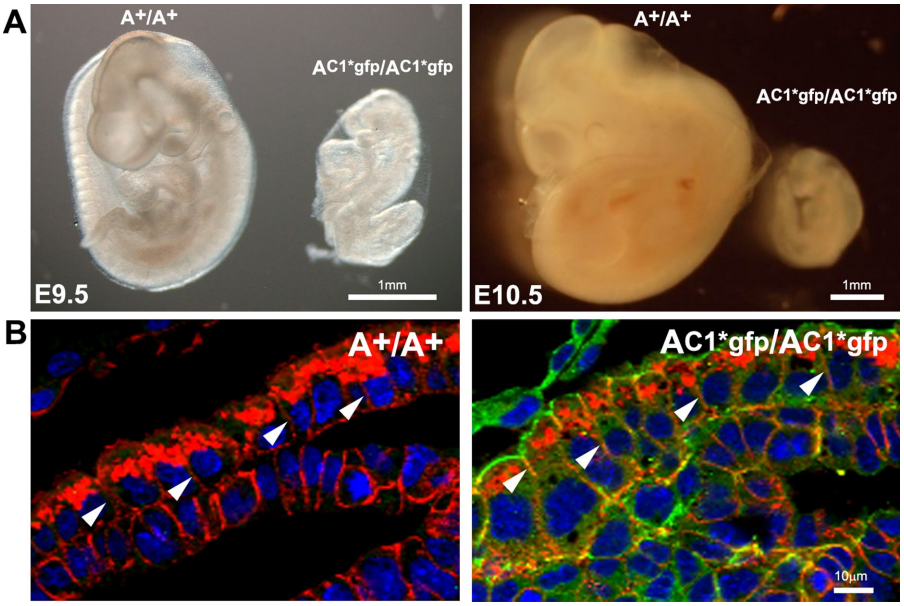

FIGURE 1: Replacing NM 2A with NM 2C1 permits embryo survival beyond gastrulation. (A) Images of E9.5 and E10.5 mouse embryos show severe growth retardation of A^{C1*gfp}/A^{C1*gfp} embryos in comparison with A^{+}/A^{+} embryos at both embryonic days. No live A^{C1*gfp}/A^{C1*gfp} embryos were collected beyond E10.5. (B) E7.5 mouse embryonic sections stained with antibodies against NM 2C (green) and E-cadherin (red) show E-cadherin localization at the adherent junctions between visceral endodermal cells (arrowheads) in A^{+}/A^{+} and A^{C1*gfp}/A^{C1*gfp} embryos. NM 2C is expressed together with E-cadherin in visceral endodermal cells of A^{C1*gfp}/A^{C1*gfp} embryos (right panel, green, arrowheads), but is not detected in A^{+}/A^{+} embryos (left panel) at E7.5.

reduced in size in comparison with A^{+}/A^{+} littermates (Figure 1A, right panel). No live A^{C1*gfp}/A^{C1*gfp} embryos were found at E11.5. Thus, in contrast to NM 2A-ablated mice, which die before E6.5, genetic introduction of NM 2C1 into mice ablated for NM 2A rescues the embryos from lethality at E6.5, allowing them to survive and undergo gastrulation.

We have previously reported that visceral endodermal cells express only NM 2A but not 2B or 2C. Global ablation of NM 2A resulted in delocalization of E-cadherin from cell–cell adhesions in the visceral endoderm. A^{-}/A^{-} embryos died before gastrulation due to a failure in functional visceral endoderm formation. As shown in Figure 1B (left panel), E-cadherin is localized to the visceral endodermal cell–cell junctions in A^{+}/A^{+} embryos (Figure 1B, left panel, red, arrowheads). Loss of NM 2A results in the absence of E-cadherin at these junctions (Conti *et al.*, 2004). Figure 1B (right panel) shows that A^{C1*gfp}/A^{C1*gfp} embryos at E7.5 develop a normal extraembryonic single cell layer of columnar visceral endoderm with NM 2C1 (in place of NM 2A) concentrated at the cell–cell junctions (green, arrowheads). Note that NM 2C1 (green) is not detected in wild-type E7.5 embryos, as manifested by lack of green signaling following immunostaining with antibodies against NMHC 2C (Figure 1B, left panel). Together, these data show that NM 2C1 can replace NM 2A to maintain functional cell–cell adhesion during visceral endoderm formation, thereby supporting mouse embryonic development throughout gastrulation.

To understand the cause of lethality in A^{C1*gfp}/A^{C1*gfp} embryos at E11–11.5, we examined placenta formation. Placentas of E9.5 A^{C1*gfp}/A^{C1*gfp} embryos appeared much smaller than those of A^{+}/A^{+} littermates. H&E staining of sagittal sections of A^{+}/A^{+} and A^{C1*gfp}/A^{C1*gfp} placentas showed that at E9.5 the labyrinth layers of A^{+}/A^{+} placentas were well expanded, with the normal trilaminar architecture (Figure 2a, enlarged panel b). The A^{+}/A^{+} labyrinth layer has a porous appearance containing a well-organized network of side-by-side fetal capillaries and maternal blood sinuses, which is required for efficient oxygen and nutrient exchange (Figure 2b). In contrast, the A^{C1*gfp}/A^{C1*gfp} placentas were much thinner and more compact, with a poorly developed labyrinth (Figure 2, c and d). The thickness of the placenta is 150.9 ± 34.0 μm and 280.0 ± 23.2 μm for A^{C1*gfp}/A^{C1*gfp} ($n = 2$) and A^{+}/A^{+} ($n = 3$) embryos, respectively ($p < 0.05$), as measured from H&E sections of one E9.5 litter. In the A^{C1*gfp}/A^{C1*gfp} labyrinth layer, blood vessels on both the maternal and fetal sides were dilated, showing almost complete loss of intermingling of fetal and maternal blood vasculatures and no expansion of the labyrinth layer, indicating a compromised vasculature invasion. These abnormalities in the placenta very likely contribute to the premature lethality.

Allantois explants confirm the requirement for NM 2A in vascular formation

The allantois is the embryonic precursor of the umbilical cord in mammals and is one of several embryonic regions that undergo vasculogenesis, the de novo formation of blood vessels. Studies have shown that vasculogenesis and angiogenesis (the remodeling and pruning of the network into specific arteries and veins) are essential for allantois function in the establishment of the chorioallantoic placenta (Downs *et al.*, 2001; Arora and Papaioannou, 2012). We made use of the allantois to study vascular formation in the mutant mice to gain insight into the formation of the placenta.

We first examined the expression pattern of the three NM 2s in allantois explants in vitro. Immunostaining of the three NM 2s was carried out in the wild-type allantois explants cultured for 24 h. Both NM 2A and NM 2B, but not NM 2C, are detected in the allantois explants (Supplemental Figure S2). Endothelial cells indicated by the costaining with CD31 (Arora and Papaioannou, 2012) express both NM 2A and NM 2B (Supplemental Figure S2). Staining of E7.5 mouse embryonic sections confirms the expression of NM 2A and 2B, but not 2C, in the developing mouse allantois in vivo (Supplemental Figure S3).

Allantoides from E8.5 wild-type and mutant embryos were dissected and cultured for 24 h in a medium containing 50% serum (Downs *et al.*, 2001). Compared with the well-organized, interconnected endothelial vascular network found in A^{+}/A^{+} littermate explants, endothelial networks of A^{C1*gfp}/A^{C1*gfp} allantois explants were significantly less complex, with fewer branches and larger gaps between the branches (Figure 3A, CD31 staining for endothelial cells; quantified in 3B). This result indicates that NM 2A plays an important role in placental vascular formation and NM 2C1 cannot replace this function of NM 2A. However, the A^{C1*gfp}/A^{C1*gfp} allantois still developed endothelial networks in explants (Figure 3A, bottom panels), which indicates that NM 2B and/or 2C may partially compensate for the loss of 2A in vascular formation. We next examined vascular network formation in wild-type allantois explants treated

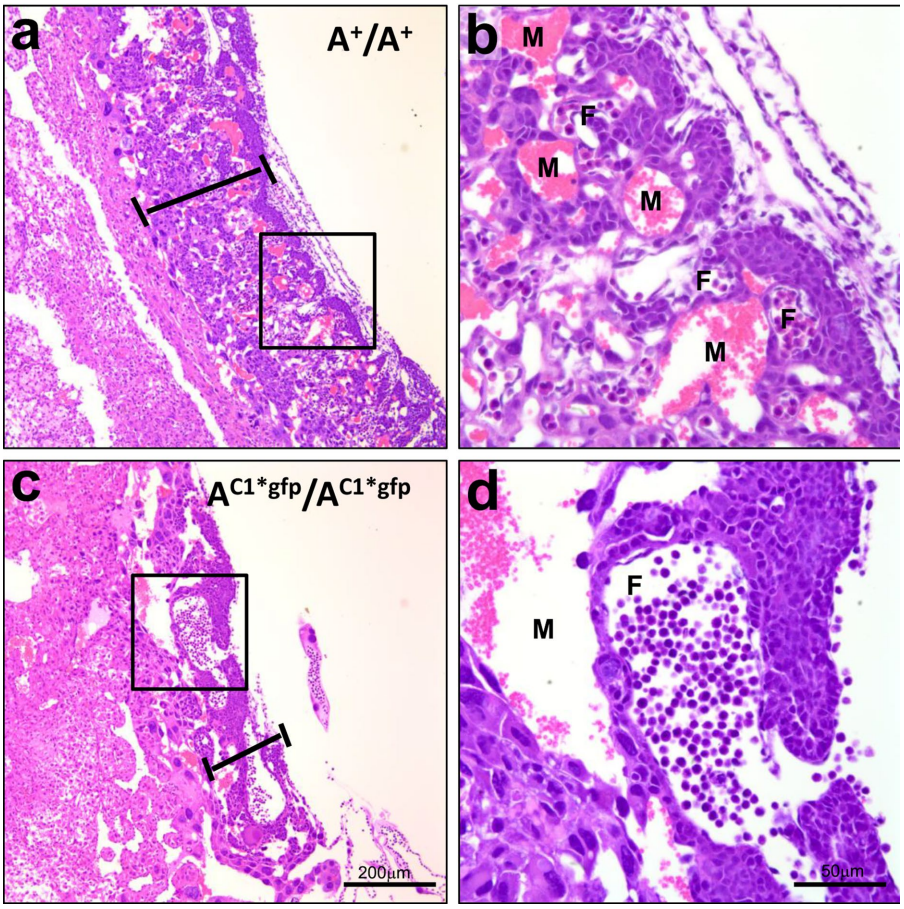

FIGURE 2: Premature death in A^{C1*gfp}/A^{C1*gfp} embryos is due to abnormalities in the placenta. H&E staining of E10.5 mouse placenta sections shows a thinner and unexpanded placenta in the A^{C1*gfp}/A^{C1*gfp} embryo (c, enlarged in d) than in an A^{+}/A^{+} littermate (a, enlarged in b). A^{C1*gfp}/A^{C1*gfp} blood vessels on both the maternal (M) and fetal (F) sides were dilated with no vascularization and no expansion of the labyrinth layer. Brackets in left panels indicate sizes of labyrinth layers. M, maternal blood vessel; F, fetal blood vessel.

with the pan-NM 2 inhibitor blebbistatin. Blebbistatin inhibits NM 2 (all paralogues) activity by blocking the myosin head from switching from the weak actin-bound state to the strong-bound state during cross-bridge cycling. As shown in Figure 3C, blebbistatin inhibited branching morphogenesis in explants. Therefore, NM 2B and/or 2C partially support placental vascular formation in the absence of NM 2A, especially in allantois explants. However, this function of NM 2B and/or 2C is not sufficient for normal placental vascular development in vivo.

NM 2C1 fails to support persistent cell migration in MEF cells

The failure of the A^{C1*gfp}/A^{C1*gfp} blood vessels to invade the labyrinthine layer implies that the impaired vascularization might result from a defect in vascular cell migration. We therefore examined the outgrowth migration rate of MEF cells from embryonic explants to see whether cell migration of A^{C1*gfp}/A^{C1*gfp} MEFs is affected. Embryonic tissues were dissected from E9.5 wild-type or mutant embryos. After attachment of the explants to a glass-bottomed dish, MEFs migrate out of the explants as a cell sheet (Figure 4A). The progression of MEF cell migration was recorded by time-lapse microscopy. Surprisingly, compared with A^{+}/A^{+}, A^{C1*gfp}/A^{C1*gfp} MEFs displayed a 2.5-fold increase in the rate of migration (A^{+}/A^{+}, 10.04 ± 4.29 μm/h; A^{C1*gfp}/A^{C1*gfp}, 25.68 ± 3.91 μm/h; Figure 4B). However, in a transwell assay to examine the directional migration of starved cells toward serum, the number of A^{C1*gfp}/A^{C1*gfp} MEFs migrating through 8-μm transwell pores after 24 h was significantly smaller than that of A^{+}/A^{+} MEFs (Figure 4C, quantified in Figure 4D). Thus, MEF cells expressing NM 2C1 in place of NM 2A migrate more rapidly than wild-type cells on a 2D surface but are not as persistent as wild-type cells in the path of migration, as measured in a transwell assay.

A^{C1*gfp}/A^{C1*gfp} MEF cells display disorganized stress fibers and form fewer and immature focal adhesions

To further investigate the mechanism underlying the impaired cell migration of the A^{C1*gfp}/A^{C1*gfp} cells, we examined the actin cytoskeletal structure and focal adhesions in the MEF cells, since these play essential roles in cell migration. MEF cells were isolated from E9.5 A^{C1*gfp}/A^{C1*gfp} embryos and cultured for in vitro studies. Actin stress fibers and focal adhesions were visualized by staining with phalloidin and antibodies to the focal adhesion markers vinculin and paxillin. For some of the experiments, we compared A^{C1*gfp}/A^{C1*gfp} MEF cells with the A^{gfp}/A^{gfp} MEFs, which have GFP fused to the endogenous NMHC 2A (Zhang *et al.*, 2012). A^{gfp}/A^{gfp} mice show no abnormalities and these MEFs are considered control cells. Except for thick actin bundles at the lateral edges of the cells, A^{C1*gfp}/A^{C1*gfp} MEF cells developed fewer stress fibers, which are thinner and sometimes disorganized within the cell body (Figure 5, bottom panels) in comparison with A^{gfp}/A^{gfp} MEFs (Figure 5, top panels).

Immunostaining for vinculin, a component of focal adhesion plaques that are involved in linkage of integrin adhesion molecules to the actin cytoskeleton, showed abundant and robust focal adhesions in the A^{+}/A^{+} MEFs (Figure 6A, left panel, arrows). In comparison with A^{+}/A^{+} cells, focal adhesions were fewer and smaller in A^{C1*gfp}/A^{C1*gfp} MEFs (Figure 6A, right panel, arrows). We quantified focal adhesion density and area in A^{+}/A^{+} and A^{C1*gfp}/A^{C1*gfp} MEFs and found that A^{+}/A^{+} cells contained significantly more focal adhesions per cell than A^{C1*gfp}/A^{C1*gfp} cells (240 ± 132 vs. 72 ± 22 per cell, $p < 0.05$, Figure 6B, top panel). The area occupied by focal adhesions in A^{+}/A^{+} cells was also significantly larger (median: 22.3 μm^2, $n = 959$ in A^{+}/A^{+} cells vs. 19.2 μm^2, $n = 430$ in A^{C1*gfp}/A^{C1*gfp} cells, $p < 0.005$, Figure 6B, bottom panel). In addition, immunostaining for phospho-Tyr118-paxillin, which indicates paxillin activation and focal adhesion maturation (Zaidel-Bar *et al.*, 2007), also revealed a reduction in focal adhesion maturation in A^{C1*gfp}/A^{C1*gfp} MEFs (Figure 6C, right panel) compared with A^{+}/A^{+} cells (Figure 6C, left panel). Immunoblotting of phospho-Tyr118-paxillin and paxillin protein expression levels in MEFs confirmed the decreased level of phospho-Tyr118-paxillin in A^{C1*gfp}/A^{C1*gfp} MEFs (32.7 ± 15.8% of the wild-type MEFs, $n = 3$, $p < 0.01$), while the total paxillin expression levels were the same (Figure 6D). In polarized cells, particularly, phospho-Tyr118-paxillin staining is weak and only detected at the

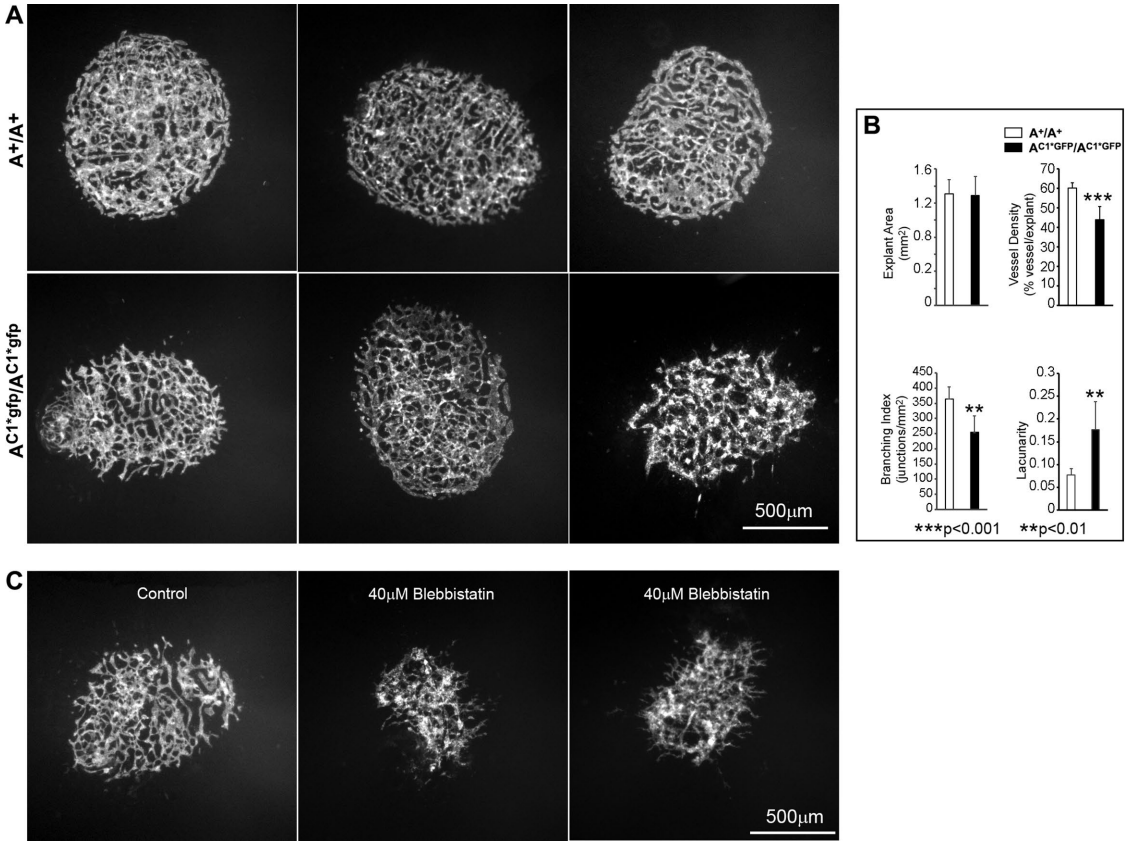

FIGURE 3: NM 2A is required in allantois explant vessel formation. (A) Epifluorescence images of CD31 stained A^{C1*gfp}/A^{C1*gfp} explants show less complex endothelial networks (vascular plexus) (bottom panels) than images of A^{+}/A^{+} explants (top panels). (B) AngioTool analysis of vascular morphology of allantois explants shows reduced vessel density and branching index and an increased lacunarity (indicating empty space) in A^{C1*gfp}/A^{C1*gfp} explants than in A^{+}/A^{+} explants. There is no significant difference in the total area of vessel explants between A^{+}/A^{+} and A^{C1*gfp}/A^{C1*gfp} explants. (C) Treatment of A^{+}/A^{+} explants with 40-μM blebbistatin blocks vascular morphogenesis.

periphery of immature focal adhesions in A^{C1*gfp}/A^{C1*gfp} MEFs (Figure 6C, right panel, arrows) in contrast to A^{+}/A^{+} cells (6C, left panel). These results indicate that NM 2C1 cannot replace the specific roles of NM 2A in actomyosin cytoskeletal organization and in focal adhesion formation and maturation.

NM 2 paralogues demonstrate different subcellular localizations and actomyosin dynamics

The introduction of NM 2C into wild-type MEF cells to generate A^{C1*gfp}/A^{+} MEF cells offers the possibility of investigating the distribution of all three NM 2 paralogues within a single cell using superresolution microscopy. We first compared the localization of NM 2C with that of NM 2A and 2B (Figure 7A). The distribution of NM 2A and 2B in A^{C1*gfp}/A^{+} MEFs is similar to that previously reported in other types of cells (Maupin *et al.*, 1994; Kolega, 1998; Saitoh *et al.*, 2001; Sandquist *et al.*, 2006; Vicente-Manzanares *et al.*, 2008). Similar to NM 2A (Figure 7Ab), NM 2C localizes toward the front of a migrating MEF cell, but NM 2C localization extends farther back into the middle of the cell than does that of NM 2A (Figure 7Ac). This is clearly seen in the green staining of the Merge (Figure 7Aa). As previously reported, NM 2B localized toward the rear of a migrating cell (Figure 7Ae). NM 2B also colocalizes with NM 2C (see Merge, Figure 7Ad); however, NM 2C expression extends much farther toward the front of the migrating cell than that of NM 2B (Figure 7A, d–f). Supplemental Figure S4 shows a single channel of the NM 2 signals using fire-scale (a colored scale of ImageJ, top right of the figure), revealing the relative intensity of individual NM 2 distribution in migrating cells and confirming the localizations above.

Figure 7B, c and f, depicts the various types of stress fibers found in the actin cytoskeleton of MEF cells, including dorsal stress fibers (dSF), ventral stress fibers (vSF), and transverse arcs (TA). Arrows in Figure 7B, c and f, illustrate examples of each of these. Whereas none of the myosin paralogues clearly localize to the dorsal stress fibers, the transverse arcs contain both NM 2A (Figure 7Ba) and NM 2C (Figure 7B, b and e), but only small amounts of NM 2B (Figure 7Bd). The immature transverse arcs at the front of the migrating cells contain more NM 2A than the relatively rear-positioned mature transverse arcs (Figure 7Ba). The NM 2C level is not markedly different between the two groups of the transverse arcs (Figure 7B, b and e). The ventral stress fibers (vSF, red arrows, Figure 7B, c and f) contain all three NM 2 paralogues (Figure 7B, a, b, d, and e). Therefore, NM 2A is mostly enriched in immature transverse arcs, NM 2B is enriched in ventral stress fibers, and in contrast to NM 2A and 2B, NM 2C is relatively abundant in mature transverse arcs. The distribution of NM 2 paralogues shown in this figure is also compatible with cofilament formation.

To better define the role of NM 2C in regulating cytoskeletal organization and focal adhesion formation, we examined the dynamics of NM 2C1 and NM 2A by FRAP analysis in MEFs expressing NM 2C1-GFP or GFP-NM 2A isolated from A^{C1*gfp}/A^{C1*gfp} and A^{gfp}/A^{gfp} mouse embryos, respectively. Compared with NM 2A, NM 2C shows a marked increase in stability, as manifested by a significantly

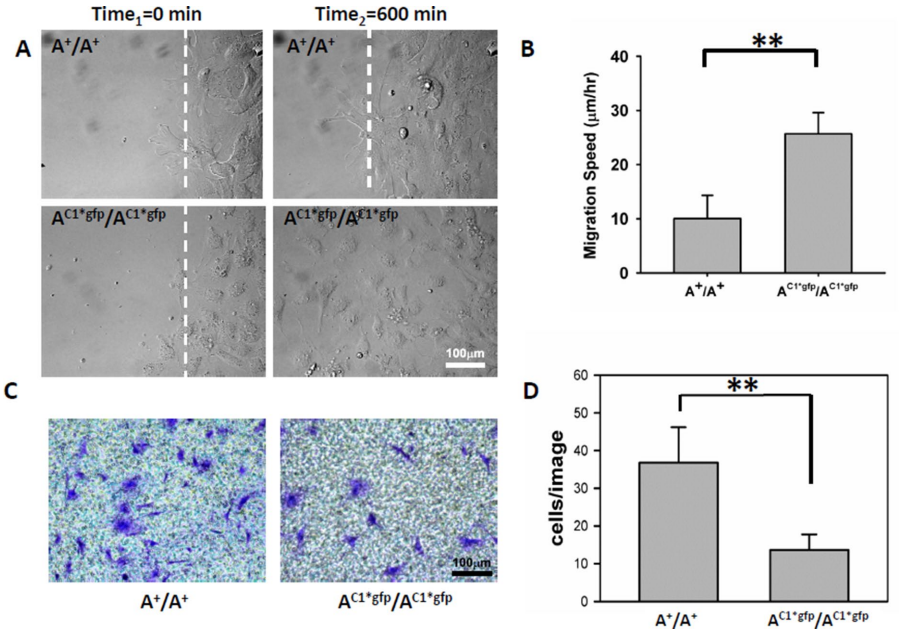

FIGURE 4: A^{C1*gfp}/A^{C1*gfp} MEF cells exhibit abnormal cell migration. (A) Representative images from time-lapse microscopy show MEF cells migrating from A^{+}/A^{+} and A^{C1*gfp}/A^{C1*gfp} embryonic explants at different time points. Cells are migrating from right to left. (B) Quantification of migration speeds (mean ± SD) shows an increased migration speed of A^{C1*gfp}/A^{C1*gfp} MEF cells in comparison with A^{+}/A^{+} cells (**$p < 0.001$, $N = 15$ and 21 cells, respectively). (C) Representative images of individual MEF cells following the transwell migration assay show that fewer A^{C1*gfp}/A^{C1*gfp} MEF cells migrate through the membrane than A^{+}/A^{+} cells. (D) Bar chart shows quantification of MEF cells migrating through a transwell membrane (**$p < 0.001$, $n = 8$ and 10 assays, respectively).

slower recovery of the signal following photobleaching (Figure 8, A and B) and a marked reduction of the mobile fraction (Figure 8C). These results indicate that NM 2C in the actomyosin cytoskeleton is much more stable than NM 2A. The actomyosin cytoskeleton is the key regulator of focal adhesion formation and maturation, and changes in the actin cytoskeletal dynamics have a profound effect on focal adhesions (Parsons *et al.*, 2010). It is likely that both the dynamics and the cellular localization of the three paralogues contribute to their specific functions in regulating cell migration.

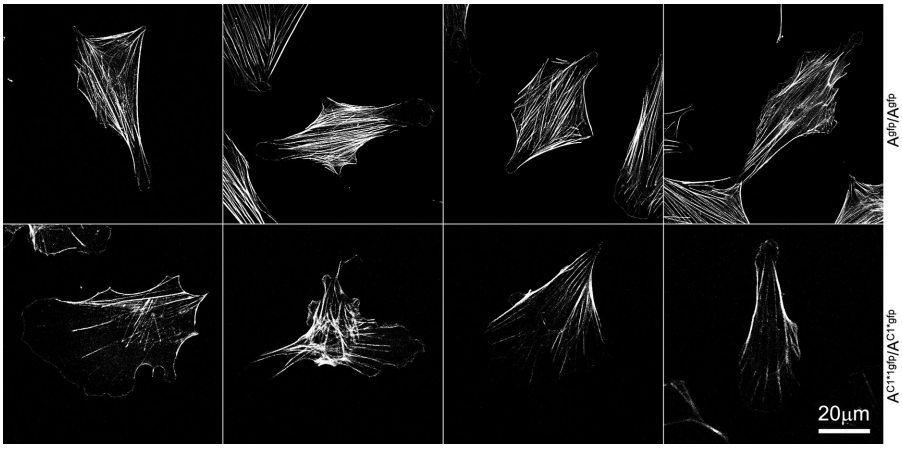

FIGURE 5: A^{C1*gfp}/A^{C1*gfp} MEF cells display disorganized stress fibers. MEF cells were stained with phalloidin to show actin filaments. Owing to great variations in MEF cell morphology, we show four representative cells for each genotype. In comparison with A^{gfp}/A^{gfp} MEFs (top), A^{C1*gfp}/A^{C1*gfp} cells show thinner and disorganized stress fibers (bottom).

DISCUSSION

Among the three NM 2 paralogues, NM 2C expression is more limited than that of NM 2A and 2B in mice. It is primarily detected at the apical borders of cell–cell junctions in mature epithelial cells, which implies a role for NM 2C at these junctions (Golomb *et al.*, 2004; Ma *et al.*, 2010). Mice ablated for NM 2C, however, are healthy and show no defects at these cell–cell junctions (Ma *et al.*, 2010). This is most likely due to its overlapping with NM 2A expression in epithelial cells. Of note is a study of the apical junctional complex of epithelial cells present in the ear organ of Corti, which contains both NM 2C and 2B. Genetic ablation of NM 2C resulted in increased expression of both NM 2A and 2B at the junction, suggesting a potential compensatory effect (Ebrahim *et al.*, 2013). This kind of compensation was not seen in the mice ablated for NM 2A and 2B.

A potential ancillary role for NM 2C is seen in the double ablation of 2B and 2C in mice. Ablation of 2B alone results in an increase in premature binucleation in cardiac myocytes, whereas ablation of both NM 2B and 2C result in defects in karyokinesis, including abnormal chromatid segregation and mitotic spindle formation (Ma *et al.*, 2010). Moreover, NM 2C1 has been shown to be required for the completion of cytokinesis in the A549 lung tumor cell line. In this case, neither NM 2A nor 2B could rescue the absence of NM 2C1 in the abscission step following small interfering RNA (siRNA) lowering of 2C1, although NM 2C0, the isoform lacking the alternative exons, was able to partially rescue abscission (Jana *et al.*, 2006). Visceral endoderm cells express only a single NM 2 paralogue, NM 2A, which is essential for maintaining E-cadherin–mediated cell–cell junctions between the endodermal cells (Conti *et al.*, 2004).

Genetic replacement of NM 2A with NM 2C1 in mice provided a unique tool for studying the function of NM 2C1 in vivo. Our results provide evidence that NM 2C1 is capable of supporting the formation of a functional visceral endoderm through maintenance of cell–cell adherent junctions, which is crucial for gastrulation during embryonic development. However, neither NM 2C1 (this report) nor NM 2B (Wang *et al.*, 2010) can replace NM 2A's role in the vascular development of the placenta. This accounts for why these mutant embryos cannot survive beyond E10.5.

NM 2C is not normally expressed in mesenchymal cells (Ma *et al.*, 2010). Unlike epithelial cells, mesenchymal cells usually do not form cell–cell adhesions; instead they form extensive cell–matrix focal adhesions required for cell locomotion. NM 2A plays an important role in focal adhesion formation and maturation in MEF cells, and MEF cells expressing NM 2C1 in place of 2A (prepared from A^{C1*gfp}/A^{C1*gfp} mice) enabled us to test the function of NM 2C1 in mesenchymal cells in culture.

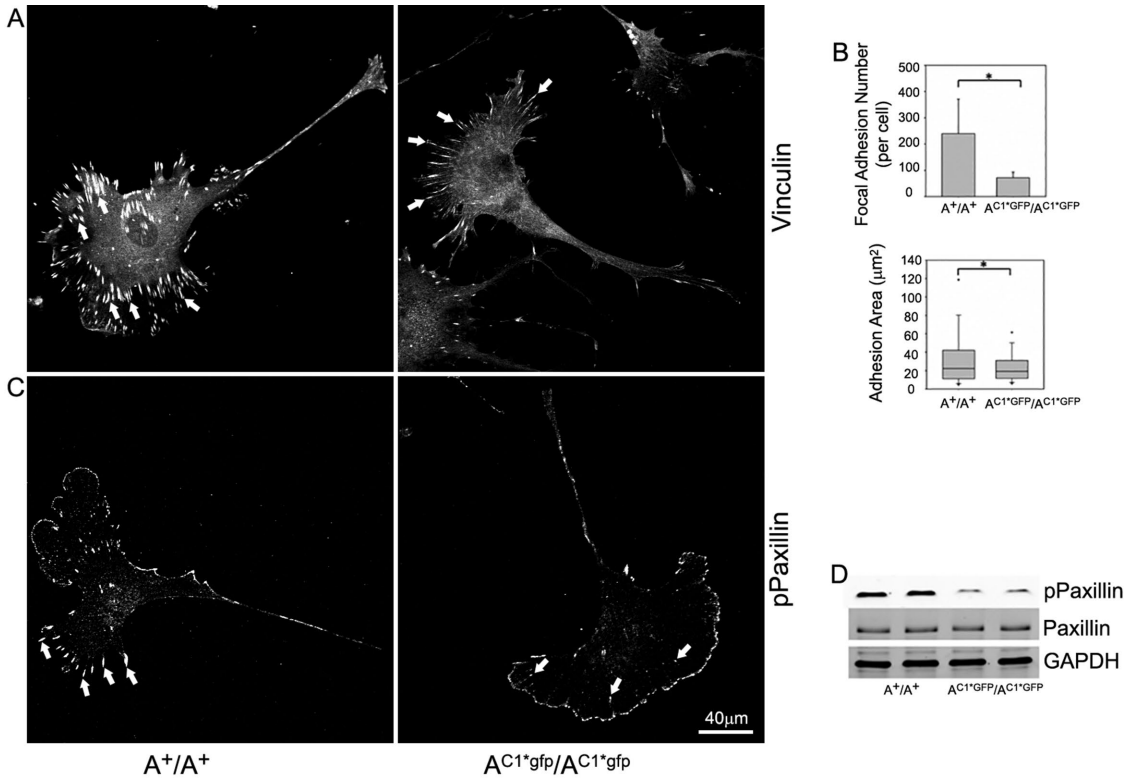

FIGURE 6: A^{C1*gfp}/A^{C1*gfp} MEF cells display fewer and smaller focal adhesions. (A) MEF cells stained with antibodies against vinculin show abundant vinculin-positive focal adhesions throughout A^+/A^+ cells (arrows, left panel). Fewer and smaller focal adhesions are detected in the A^{C1*gfp}/A^{C1*gfp} MEF cells (arrows, right panel). (B) Quantification of focal adhesion numbers and adhesion area (box plot) in A^+/A^+ and A^{C1*gfp}/A^{C1*gfp} cells from A (*$p < 0.05$). (C) MEF cells stained for phosphopaxillin show a marked decrease in phosphopaxillin staining at focal adhesions in A^{C1*gfp}/A^{C1*gfp} cells (right panel, arrows) in comparison with A^+/A^+ cells (left panel, arrows). (D) Immunoblots show that compared with A^+/A^+ MEFs, the expression level of phosphopaxillin is reduced to 32.7 ± 15.8% of the A^+/A^+ MEF cell level in A^{C1*gfp}/A^{C1*gfp} MEFs ($n = 3$, $p < 0.01$), while the expression level of total paxillin remains the same. GAPDH is used as a control for loading.

A^{C1*gfp}/A^{C1*gfp} MEF cells expressing NM 2C1 at a level roughly equivalent to the endogenous NM 2A level, however, failed to form mature focal adhesions, which resulted in a defect in persistent cell migration in a transwell assay. These defects most likely reflect the differences in NM 2C1 myosin kinetics and cellular localization from NM 2A, since the former is a slower motor (Kim *et al.*, 2005) and does not turn over as quickly, as shown in this report. Moreover, in polarized, migrating cells NM 2C1 localizes differently than NM 2A, extending more toward the middle of the cell compared with NM 2A which is closer to the leading edge, and becomes the most prominent NM 2 paralogue decorating the stress fiber, in this case the transverse arcs. Defects in cell migration and focal adhesion formation observed in A^{C1*gfp}/A^{C1*gfp} MEF cells were also seen in MEF cells expressing NM 2B in place of 2A (Wang *et al.*, 2010), as well as in foreskin fibroblast cells following siRNA knockdown of NM 2A expression (Even-Ram *et al.*, 2007). Therefore, defects seen in A^{C1*gfp}/A^{C1*gfp} MEF cells are largely due to a loss of NM 2A function. Our present study demonstrates a unique requirement for NM 2A in efficient cell migration. These specific properties of NM 2A may also explain why it is essential and cannot be replaced by other NM 2 paralogues for placental vascular formation during mouse embryonic development.

An important finding from these NM 2 swapping experiments is the differential requirement for NM 2 in cell–cell adherent adhesions versus cell–matrix focal adhesions. All three NM 2 paralogues are interchangeable in the maintenance of cell–cell adhesions, while NM 2A is uniquely required for focal adhesion maturation in MEF cells. In addition, whereas cell–cell adhesion does not require full NM 2 motor activity (Ma *et al.*, 2007), focal adhesions are sensitive to NM 2 motor activity.

MATERIALS AND METHODS

Generation of NM 2C1 replacement of NM 2A in mice

All mouse procedures were carried out in accordance with National Heart, Lung, and Blood Institute (NHLBI) Animal Care and Use Committee guidelines. As shown in Supplemental Figure S1, to generate the genetic replacement of NM 2A with NM 2C1 in mice, standard homologous recombination methods were used. Mouse NMHC 2C1 cDNA with the GFP sequence fused to its C-terminus was targeted into exon2, the first coding exon of *Myh9* just 5′ of the initiating ATG codon. Fragments flanking exon2 were amplified from a 129S6/SvEv genomic BAC clone harboring the complete *Myh9* locus. In the targeting construct, the 5′ arm, ~4 kb immediately upstream of the initiating ATG codon in exon2 was followed by a cDNA cassette encoding mouse NMHC 2C1-GFP with the EGFP sequence (Stratagene) at the 3′-end of the mouse NMHC 2C1 sequence, followed by SV40 polyA, a loxP-flanked PGK-Neo^r cassette, and the ~2 kb genomic sequence 3′ of the ATG codon. Nucleotide sequences of the cloned DNA fragments were confirmed by sequencing. The transfection of mouse 129 strain embryonic stem (ES) cells and the generation of chimeric mice were performed at the

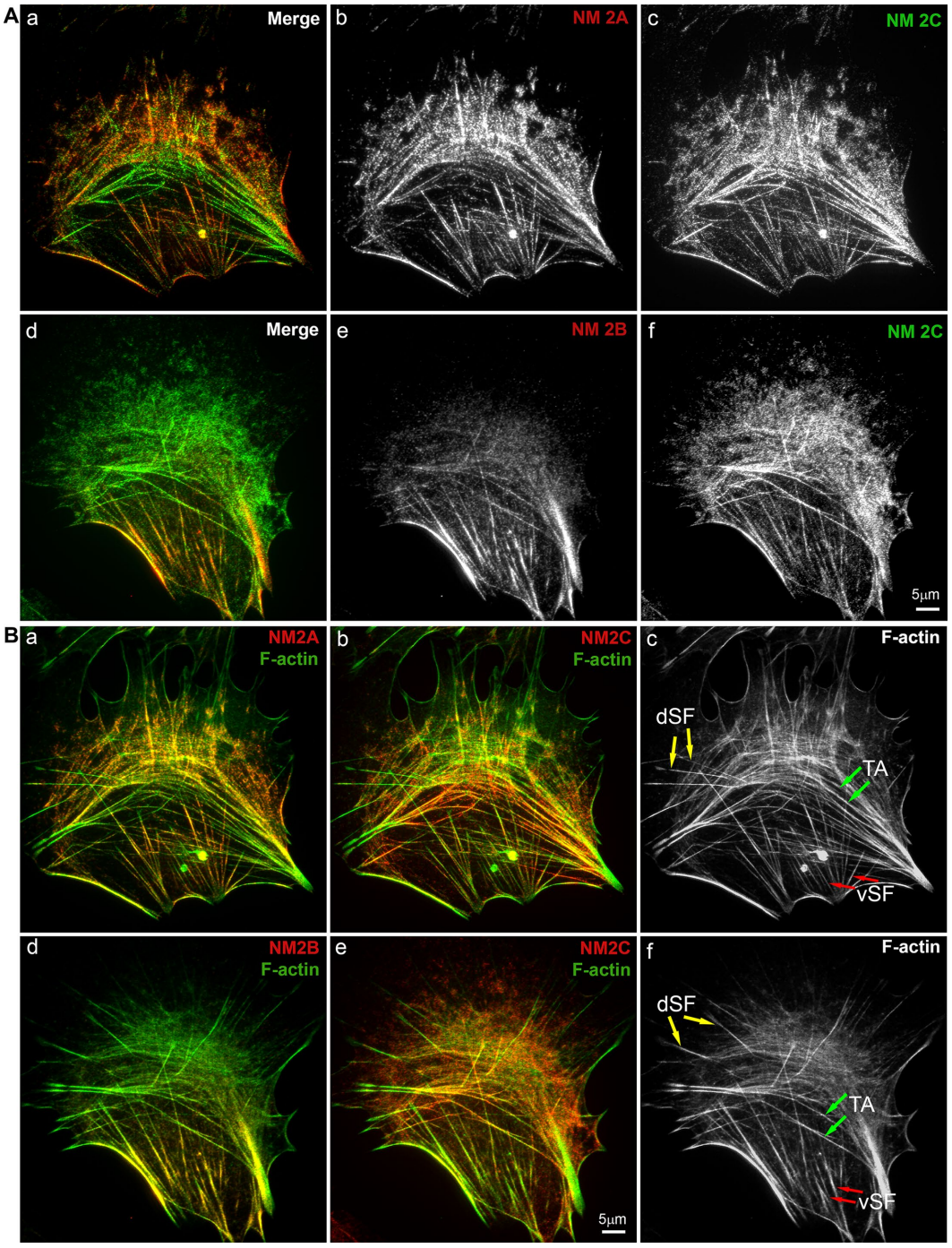

FIGURE 7: Localization of three NM 2s in A^{C1*gfp}/A^{+} MEF cells. (A) Superresolution microscopy images of A^{C1*gfp}/A^{+} MEF cells stained with antibodies for NM 2A (red, 7Ab) or NM2B (red, 7Ae) and GFP (green, indicating NM 2C, 7Ac,f). Aa is a merge of NM 2A (b) and NM 2C (c), and Ad is a merge of NM 2B (e) and NM 2C (f). (B) iSIM images of A^{C1*gfp}/A^{+} MEF cells stained with phalloidin (green, for stress fibers) and antibodies for individual NM 2s. Panels Bc and Bf show a single channel of phalloidin staining to illustrate dorsal stress fibers (dSFs, yellow arrows), ventral stress fibers (vSFs, red arrows), and transverse arcs (TAs, green arrows). Both NM 2A (a) and NM 2C (b) localize with transverse arcs (TAs). All three NM 2s localize to ventral stress fibers (vSF), but NM 2B is particularly concentrated in vSF. No NM 2s localize with the dorsal stress fibers (dSF).

NHLBI Transgenic Mouse Core Facility by conventional methods. Positive ES cell clones were determined by Southern blot. The genotype of the initial mutant mice was confirmed by Southern blotting and subsequent genotyping was routinely performed by PCR. The Neo^{r} cassette, which aided in selection of targeted clones, was removed by crossing the mutant mice with CMV-Cre mice (BALB/c-Tg(CMV-cre)1Cgn/J, Jax 003465). Mice are available at the Mutant Mouse Resource & Research Centers, ID#41404.

Immunoblotting

Immunoblotting was performed as described by Zhang *et al*. (2012), with the exception that proteins were transferred to nitrocellulose

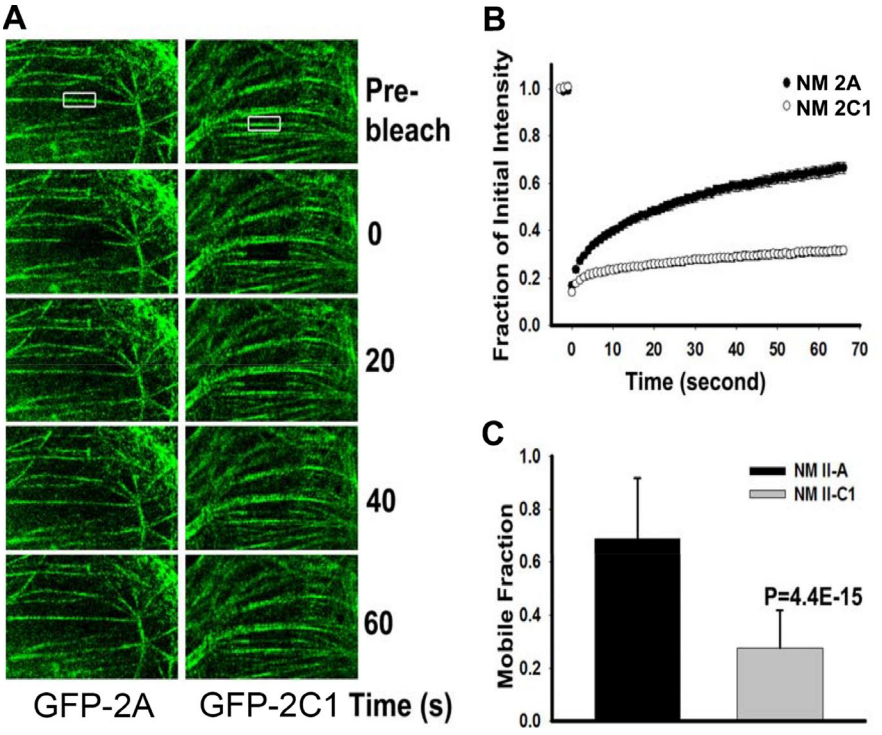

FIGURE 8: Fluorescence recovery after photobleaching (FRAP) analysis of GFP-NM 2A and NM 2C1-GFP in MEF cells. (A) Representative images for GFP signals (green) following photobleaching at different time points during recovery. The boxes in the two top panels indicate the area bleached. (B) Recovery curves of GFP signals show a slow recovery of NM 2C1-GFP in comparison with GFP-NM 2A. (C) Bar graphs of the calculated mobile fraction of GFP signals show a significant decrease in the mobile fraction of NM 2C1-GFP in comparison with GFP-NM 2A ($n = 20$ each).

membranes (Invitrogen). Signal was detected with fluorescence-linked secondary antibodies on a Li-Cor Odyssey infrared imager. Primary antibodies were NMHC 2A (1:50,000; BioLegend), NMHC 2C (1:5000; BioLegend), GFP (1:5000; Abcam), p-paxillin (1:1000; BD Transduction Laboratories), paxillin (1:20,000; BD Transduction Laboratories), and GAPDH (1:5000; Meridian).

Tissue preparation

Histological analyses of placentas and embryos were performed as described previously (Zhang *et al.*, 2012). In brief, placentas and embryos at E9.5 were fixed with 4% paraformaldehyde (PFA) in phosphate-buffered saline (PBS), pH 7.4. They were then embedded in paraffin, sectioned, and stained with hematoxylin and eosin (H&E). For immunostaining, paraffin sections were dewaxed, rehydrated, subjected to microwave antigen-retrieval in 10-mM sodium citrate (Sigma Aldrich), blocked with 1% bovine serum albumin (BSA), 5% goat serum in PBS, and then incubated with primary antibodies at 4°C overnight, followed by incubation with AlexaFluor 488 or 594-conjugated goat anti-mouse or anti-rabbit immunoglobulin G (IgG) (Molecular Probes, 1:200) at room temperature for 1 h. Nuclei were stained with DAPI (Molecular Probes; 1:1000). The slides were mounted with Prolong Antifade (Invitrogen) for confocal imaging.

Isolation, culture, and immunofluorescence of MEFs

A^+/A^+, A^{C1*gfp}/A^+, and A^{C1*gfp}/A^{C1*gfp} MEFs were isolated from embryos at E9.5 from crosses of heterozygous A^{C1*gfp}/A^+ mice and genotyped with genomic DNA isolated from yolk sacs. MEFs were maintained in high-glucose DMEM (Life Technologies) plus 10% fetal bovine serum (FBS; Life Technologies) at 37°C, cultured for three passages, and then used for most experiments. For immunofluorescence staining, cells were grown overnight on chamber slides, washed with PBS (warmed to 37°C), fixed with 4% PFA, and then permeabilized with 0.5% Triton X-100 (Sigma Aldrich). The fixed cells were blocked with 1% BSA plus 5% goat serum in PBS and then incubated with antibodies against NMHC 2A, 2B, vinculin (1:1000; Sigma), phospho-Tyr118-paxillin (1:100; BD Biosciences, pY118) at 4°C overnight, followed by incubation with AlexaFluor 405, 488 or 594–conjugated goat anti-mouse or anti-rabbit IgG (1:200; Molecular Probes) at room temperature for 1 h. Actin filaments and nuclei were stained with AlexaFluor 594–conjugated phalloidin (1:200; Molecular Probes) and DAPI (1:1000; Molecular Probes), respectively. The slides were mounted with Prolong Antifade (Invitrogen) for confocal imaging.

Cell migration assays

Embryonic explants at E9.5 were cultured in high-glucose DMEM plus 10% FBS at 37°C. After the explants attached to the coverslip, MEF cell outgrowth from the explants was recorded for 16 h using an inverted microscope (Olympus IX-70) equipped with an environmental chamber set at 37°, 5% CO_2. Migration speed was calculated from the distance the MEFs migrated, divided by the time used for recording the distance, and expressed as mean ± SD.

Transwell migration assays

Transwell migration assays were performed using Corning Transwells (Sigma Aldrich; 24-well cell culture plate, 6.5-mm-diameter inserts, 8.0-μm pore size). The lower chambers were filled with high-glucose DMEM containing 10% FBS. Samples of 1.0×10^4 cells in a total volume of 200 μl, serum-starved for 24 h, were applied to the upper chamber in serum-free DMEM. A^+/A^+ and A^{C1*gfp}/A^{C1*gfp} MEF samples were repeated 10 and eight times, respectively. The cells were allowed to migrate at 37°C and 5% CO_2 for 20 h. Transwell inserts were washed with PBS, fixed with 4% PFA, and stained with 0.2% crystal violet in 2% ethanol. Nonmigratory cells at the upper surface were removed with cotton swabs and the migrated cells attached to the lower surface were imaged with a Nikon TMS 10x air objective. Three images were taken and the number of migrated cells was averaged from each transwell insert.

Isolation and culture of allantois explants

Allantois explants were isolated from E8.5 embryos from crosses of heterozygous A^{C1*gfp}/A^+ mice and genotyped with genomic DNA isolated from embryos. Allantois explants were cultured in 24-well plates with high-glucose DMEM plus 50% FBS at 37°C for 24 h. For immunofluorescence staining, allantois explants were washed with 37°C PBS, fixed with 4% PFA, and then blocked with 1% BSA plus 5% goat serum in PBS. After blocking, allantois explants were incubated with rat anti-mouse CD31 antibodies (1:100; BD Biosciences) at 4°C overnight, followed by incubation with AlexaFluor

594–conjugated goat anti-rat IgG (1:200; Molecular Probes) at room temperature for 1 h. Round coverslips were mounted onto allantois explants before epifluorescence imaging. An AngioTool (Zudaire *et al.*, 2011) was used to characterize vessels in allantois explants following CD31 staining to reveal the vascular network.

Light, epifluorescence, confocal microscopy, and FRAP

Images of H&E tissue sections were acquired with an Olympus BX40 40 × air objective at room temperature using a SpotFlex camera. Epifluorescence images of allantois explants were acquired with Olympus IX70. Confocal immunostaining images were collected using an LSM510 META confocal microscope (Carl Zeiss). Fluorescence recovery after photobleaching (FRAP) analysis was performed using an LSM510 META confocal microscope (Carl Zeiss). Super-resolution images were captured using a Visitech Instant Structured Illumination Microscope (iSIM). In all cases, when possible, comparisons were made among littermates.

Quantification of MEF focal adhesion

Focal adhesions density (number) and size (surface area) were quantified using vinculin staining in A^{+}/A^{+} and A^{C1*gfp}/A^{C1*gfp} MEFs. Individual focal adhesions were segmented as "surface" objects using Imaris (Bitplane) software. This enabled users to review and edit the automatic segmented objects for accuracy. Statistics of the number of focal adhesions per cell and their individual surface areas per cell were exported for analysis in Excel (Microsoft) software.

Statistical analysis

Data are expressed as mean ± SD. Student's *t* test was used to test statistical significance between two groups using Sigmaplot software.

ACKNOWLEDGMENTS

We thank Sachiyo Kawamoto, Mary Anne Conti, and members of the Laboratory of Molecular Cardiology, who provided critical comments on the manuscript. Alexander Zhovmer helped with iSIM microscopic imaging. We also thank Christian A. Combs and Daniela Malide (NHLBI Light Microscopy Core). Antoine Smith and Dalton Saunders provided excellent technical assistance. This research was supported by the Division of Intramural Research, NHLBI (HL-004228).

REFERENCES

Arora R, Papaioannou VE (2012). The murine allantois: a model system for the study of blood vessel formation. Blood 120, 2562–2572.

Bao J, Ma X, Liu C, Adelstein RS (2007). Replacement of nonmuscle myosin II-B with II-A rescues brain but not cardiac defects in mice. J Biol Chem 282, 22102–22111.

Beach JR, Shao L, Remmert K, Li D, Betzig E, Hammer JA 3rd (2014). Nonmuscle myosin II isoforms coassemble in living cells. Curr Biol 24, 1160–1166.

Conti MA, Even-Ram S, Liu C, Yamada KM, Adelstein RS (2004). Defects in cell adhesion and the visceral endoderm following ablation of nonmuscle myosin heavy chain II-A in mice. J Biol Chem 279, 41263–41266.

Downs KM, Temkin R, Gifford S, Mchugh J (2001). Study of the murine allantois by allantoic explants. Dev Biol 233, 347–364.

Ebrahim S, Fujita T, Millis BA, Kozin E, Ma X, Kawamoto S, Baird MA, Davidson M, Yonemura S, Hisa Y, *et al.* (2013). NMII forms a contractile transcellular sarcomeric network to regulate apical cell junctions and tissue geometry. Curr Biol 23, 731–736.

Even-Ram S, Doyle AD, Conti MA, Matsumoto K, Adelstein RS, Yamada KM (2007). Myosin IIA regulates cell motility and actomyosin-microtubule crosstalk. Nat Cell Biol 9, 299–309.

Golomb E, Ma X, Jana SS, Preston YA, Kawamoto S, Shoham NG, Goldin E, Conti MA, Sellers JR, Adelstein RS (2004). Identification and characterization of nonmuscle myosin II-C, a new member of the myosin II family. J Biol Chem 279, 2800–2808.

Heissler SM, Manstein DJ (2011). Comparative kinetic and functional characterization of the motor domains of human nonmuscle myosin-2C isoforms. J Biol Chem 286, 21191–21202.

Heissler SM, Manstein DJ (2013). Nonmuscle myosin-2: mix and match. Cell Mol Life Sci 70, 1–21.

Jana SS, Kawamoto S, Adelstein RS (2006). A specific isoform of nonmuscle myosin II-C is required for cytokinesis in a tumor cell line. J Biol Chem 281, 24662–24670.

Jana SS, Kim KY, Mao J, Kawamoto S, Sellers JR, Adelstein RS (2009). An alternatively spliced isoform of non-muscle myosin II-C is not regulated by myosin light chain phosphorylation. J Biol Chem 284, 11563–11571.

Kim KY, Kovacs M, Kawamoto S, Sellers JR, Adelstein RS (2005). Disease-associated mutations and alternative splicing alter the enzymatic and motile activity of nonmuscle myosins II-B and II-C. J Biol Chem 280, 22769–22775.

Kolega J (1998). Cytoplasmic dynamics of myosin IIA and IIB: spatial "sorting" of isoforms in locomoting cells. J Cell Sci 111 (Pt 15), 2085–2095.

Liu T, Hu Y, Guo S, Tan L, Zhan Y, Yang L, Liu W, Wang N, Li Y, Zhang Y, *et al.* (2018). Identification and characterization of MYH9 locus for high efficient gene knock-in and stable expression in mouse embryonic stem cells. PLoS One 13, e0192641.

Liu Z, Van Rossen E, Timmermans JP, Geerts A, Van Grunsven LA, Reynaert H (2011). Distinct roles for non-muscle myosin II isoforms in mouse hepatic stellate cells. J Hepatol 54, 132–141.

Ma X, Bao J, Adelstein RS (2007). Loss of cell adhesion causes hydrocephalus in nonmuscle myosin II-B-ablated and mutated mice. Mol Biol Cell 18, 2305–2312.

Ma X, Jana SS, Conti MA, Kawamoto S, Claycomb WC, Adelstein RS (2010). Ablation of nonmuscle myosin II-B and II-C reveals a role for nonmuscle myosin II in cardiac myocyte karyokinesis. Mol Biol Cell 21, 3952–3962.

Ma X, Kawamoto S, Hara Y, Adelstein RS (2004). A point mutation in the motor domain of nonmuscle myosin II-B impairs migration of distinct groups of neurons. Mol Biol Cell 15, 2568–2579.

Maupin P, Phillips CL, Adelstein RS, Pollard TD (1994). Differential localization of myosin-II isozymes in human cultured cells and blood cells. J Cell Sci 107 (Pt 11), 3077–3090.

Parsons JT, Horwitz AR, Schwartz MA (2010). Cell adhesion: integrating cytoskeletal dynamics and cellular tension. Nat Rev Mol Cell Biol 11, 633–643.

Robinson DN, Spudich JA (2004). Mechanics and regulation of cytokinesis. Curr Opin Cell Biol 16, 182–188.

Saitoh T, Takemura S, Ueda K, Hosoya H, Nagayama M, Haga H, Kawabata K, Yamagishi A, Takahashi M (2001). Differential localization of nonmuscle myosin II isoforms and phosphorylated regulatory light chains in human MRC-5 fibroblasts. FEBS Lett 509, 365–369.

Sandquist JC, Swenson KI, Demali KA, Burridge K, Means AR (2006). Rho kinase differentially regulates phosphorylation of nonmuscle myosin II isoforms A and B during cell rounding and migration. J Biol Chem 281, 35873–35883.

Takeda K, Kishi H, Ma X, Yu ZX, Adelstein RS (2003). Ablation and mutation of nonmuscle myosin heavy chain II-B results in a defect in cardiac myocyte cytokinesis. Circ Res 93, 330–337.

Tullio AN, Accili D, Ferrans VJ, Yu ZX, Takeda K, Grinberg A, Westphal H, Preston YA, Adelstein RS (1997). Nonmuscle myosin II-B is required for normal development of the mouse heart. Proc Natl Acad Sci USA 94, 12407–12412.

Tullio AN, Bridgman PC, Tresser NJ, Chan CC, Conti MA, Adelstein RS, Hara Y (2001). Structural abnormalities develop in the brain after ablation of the gene encoding nonmuscle myosin II-B heavy chain. J Comp Neurol 433, 62–74.

Vicente-Manzanares M, Koach MA, Whitmore L, Lamers ML, Horwitz AF (2008). Segregation and activation of myosin IIB creates a rear in migrating cells. J Cell Biol 183, 543–554.

Vicente-Manzanares M, Ma X, Adelstein RS, Horwitz AR (2009). Non-muscle myosin II takes centre stage in cell adhesion and migration. Nat Rev Mol Cell Biol 10, 778–790.

Wang A, Ma X, Conti MA, Liu C, Kawamoto S, Adelstein RS (2010). Nonmuscle myosin II isoform and domain specificity during early mouse development. Proc Natl Acad Sci USA 107, 14645–14650.

Zaidel-Bar R, Milo R, Kam Z, Geiger B (2007). A paxillin tyrosine phosphorylation switch regulates the assembly and form of cell–matrix adhesions. J Cell Sci 120, 137–148.

Zhang Y, Conti MA, Malide D, Dong F, Wang A, Shmist YA, Liu C, Zerfas P, Daniels MP, Chan CC, *et al.* (2012). Mouse models of MYH9-related disease: mutations in nonmuscle myosin II-A. Blood 119, 238–250.

Zudaire E, Gambardella L, Kurcz C, Vermeren S (2011). A computational tool for quantitative analysis of vascular networks. PLoS One 6, e27385.